Nanoscale

PAPER

Cite this: *Nanoscale*, 2020, **12**, 9507

A ferromagnetic skyrmion-based diode with a voltage-controlled potential barrier†

Li Zhao, [a] Xue Liang,[a] Jing Xia,[b] Guoping Zhao*[a,c,d] and Yan Zhou [b]

Received 12th December 2019,
Accepted 26th March 2020

DOI: 10.1039/c9nr10528j

rsc.li/nanoscale

Traditional electronic technologies face many challenges, such as the scalability of equipment and improvement of performance. Some novel spintronic objects are expected to improve electronic applications for the more-than-Moore era. For example, a magnetic skyrmion is a potential building block for the next generation of electronic devices due to its small size, good stability and low driving current threshold. However, the Magnus force acting on a ferromagnetic skyrmion can induce a transverse motion perpendicular to the driving force, which may lead to the destruction of skyrmions at sample edges. Here, we computationally demonstrate that the nanotrack edge with high magnetic perpendicular anisotropy (PMA), which is controlled by the voltage-controlled magnetic anisotropy (VCMA) effect, not only enables the reliable motion of skyrmions along the nanotrack, but also increases the skyrmion velocity. The one-way motion of skyrmions can be realized by applying voltage to create high PMA at a local area near the nanotrack edge. In addition, we show a feasible design of a skyrmion diode similar to the P–N junction. Our results may provide guidelines for designing skyrmion-based diodes.

Introduction

A magnetic skyrmion is a nonlinear nanoscale spin configuration with quasi-particle-like properties, which exists in magnetic systems, such as non-centrosymmetric magnets and magnetic multilayers lacking inversion symmetry.[1–7] It has the characteristic of topological protection,[8,9] so it is not easy to be pinned by defects.[10] In addition, the size of the skyrmion is generally several nanometers to several hundred nanometers, which is conducive to the miniaturization of electronic devices and the improvement of storage density.[8–11] And compared with the traditional domain wall,[12,13] the critical driving current of the skyrmion is much smaller.[11,14,15] More importantly, the skyrmion can lay the foundation for the development of magnetic computers[16,17] outside the von Neumann architecture, which strictly separates information processing and storage. Recently the unconventional operation for probabilistic[18] and Brownian computing[19] based on skyrmions has been proved in experiments. Therefore, the skyrmion is expected to usher a new era for the spintronic devices.[20,21] More and more skyrmion-based spintronic devices have been designed, such as nanotrack memory devices,[22–25] transistors,[26–29] logic gates,[30,31] spin nano-oscillators,[32–34] neural elements[35] and resonant diodes,[36] with the in-depth study of the nucleation, motion, annihilation and detection of skyrmions.[10,37–40] In order to ultimately achieve and commercialize skyrmion-based spintronic devices, a reasonable structural model and feasible design method are essential.

The voltage-controlled magnetic anisotropy (VCMA) effect has been observed in various materials, such as Ir/CoFeB/MgO,[41] Ta/CoFeB/MgO,[42] Pt/Co[43,44] Co/Pd/MgO,[45] Pt/Co/Pd/MgO[46] and Fe/Co/MgO.[47] Relevant studies on the properties of electric field effects indicate that the VCMA effect associates with the spin-dependent screening of the electric field,[48] electric field induced changes in the band structure,[49] and changes in the electron filling of the 3d orbital caused by the charge accumulation at the interface.[50–52] Recently, several other possible mechanisms have been proposed, such as electric field induced atomic displacement at the interface between ferromagnetic oxide and dielectric subtance.[53] In 2009, Y. Suzuki *et al.* reported that a small electric field of about 100 mV nm^{-1} can change PMA by 40% with the VCMA efficiency of 210 fJ V^{-1} m^{-1} at room temperature.[54] The VCMA efficiency is the ratio between the induced PMA change and applied electric field $\frac{\Delta K_u}{\Delta E}$. Recently, Aik Jun Tan *et al.* reported that the reversible change in magnetic anisotropy at room

[a]*College of Physics and Electronic Engineering, Sichuan Normal University, Chengdu 610068, China. E-mail: zhaogp@uestc.edu.cn*
[b]*School of Science and Engineering, The Chinese University of Hong Kong, Shenzhen, Guangdong 518172, China*
[c]*State Key Laboratory of Metastable Materials Science and Technology, Yanshan University, Qinhuangdao 066004, China*
[d]*Collaborative Innovation Center for Shanxi Advanced Permanent Materials and Technology, Linfen 041004, China*

†Electronic supplementary information (ESI) available. See DOI: 10.1039/c9nr10528j

temperature can be realized by using a small gate voltage through H+ pumping, and the VCMA efficiency can be up to 5000 fJ V^{-1} m^{-1}.[55] Hence, voltage-controlled spintronic devices show great potential in feasibility. In this work, considering the feasibility of the design, we mainly use a more conservative estimate, namely 10% of the change in PMA by the electric field. Indeed, a larger change of PMA is also studied in this paper.

However, there are still some problems in the implementation of skyrmion-based diodes, which play an important role in the next generation of electronic devices. During the process of the skyrmion moving along the nanotrack, the induced Magnus force causes lateral displacement, resulting in the skyrmion Hall effect (SkHE).[8,56,57] It should be avoided in practical application as it leads to the annihilation of the skyrmion at the boundary.[37] The SkHE can be eliminated by bilayer-skyrmions,[58] counteracted by adding a high-*K* material at boundaries,[59] suppressed by reducing the thickness of the middle region[60] and so on. In our work the SkHE is suppressed by high magnetic crystalline anisotropy boundaries formed by VCMA, as shown in Fig. 1. The effect of high-anisotropy boundaries on the SkHE is significant and it is helpful to improve the skyrmion velocity, which is studied systematically in this paper.

On the other hand, how to realize the one-way motion of the skyrmion easily and practically is also a problem worth solving. As everyone knows, the motion direction of the skyrmion can be changed by the direction of the normal current injected horizontally into the heavy metal layer. Hence, the injection direction of the driving current is chosen as the control signal in the design, which is equivalent to the bias voltage in the traditional P–N junction diode.[61,62] Besides, the high-anisotropy trapezoid region near the boundary of the nanotrack formed by VCMA is used as a modulation element to achieve the one-way motion of the skyrmion. The simulation results show that the design can realize the one-way motion of the skyrmion, making the nanotrack become a P–N junction, which is investigated deeply here.

The structure of the skyrmion-based diode

Fig. 1(a) shows the diagram of a skyrmion-based diode, which comprises five parts: magnetic tunnel junction (MTJ) writers, nanotracks, MTJ readers, VCMA gates and peripheral circuits. Initially, the skyrmion is nucleated at the left/right side of the nanotrack by the MTJ writer injecting the spin polarization current. Later, it is driven by the spin current generated by the current flowing along the heavy metals.[10,63] VCMA gates are composed of a metal electrode and insulating medium, resulting in a barrier potential at boundaries and the partial middle region of the nanotrack. As a result, the skyrmion can be confined to the nanotrack and moves in one direction, as shown in Fig. 1(b). When the skyrmion safely moves to the other side, the reader can detect it according to the tunneling magnetoresistance effect (TMR).[22] Besides, the parameters for micromagnetic simulation in this paper are shown in Table 1.

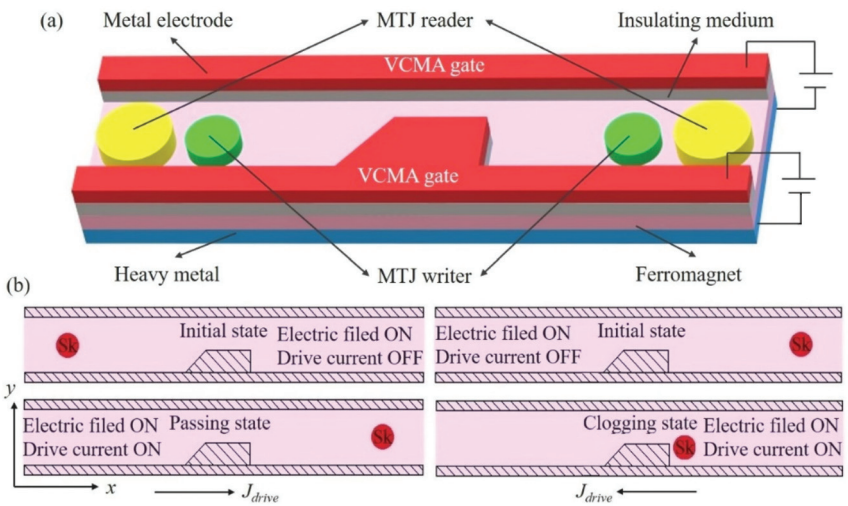

Fig. 1 (a) Schematic of the skyrmion-based diode. It mainly consists of five parts: magnetic tunnel junction (MTJ) writers, nanotracks, MTJ readers, voltage controllable magnetic anisotropy (VCMA) gates and peripheral circuits (which are not shown in the figure). VCMA gates are made up of a metal electrode and insulating medium, which improves the PMA in the region of the nanotrack by electric field. Firstly, the left/right writer with the spin polarization current nucleates the skyrmion. Afterwards, during the motion of the skyrmion, the high-anisotropy region formed by VCMA gates suppresses the lateral drift of the skyrmion. In addition, the skyrmion, moving from the left or right side of the nanotrack, is affected by the middle of the high-anisotropy region and can bypass or be clogged. Finally, the skyrmion safely passing through the nanotrack is able to be detected by the readers due to the change in tunneling magnetoresistance (TMR). (b) Schematic view (*xy*-plane) of the one-way motion of the skyrmion in the skyrmion-based diode. The pictures on the left and right correspond to the initial and final states of the skyrmion as it moves forward and reverse, respectively. The shadow part represents the high-anisotropy region (*i.e.*, the voltage-control region).

Table 1 Material parameters in the simulation corresponding to CoPt

Quantity	Value
Saturation magnetization M_s (MA m^{-1})	0.58
Exchange stiffness A (pJ m^{-1})	15
Uniaxial anisotropy constant K (MJ m^{-3})	0.8
DMI constant D (mJ m^{-2})	3
Damping coefficient α	0.1
Polarizability rate P	0.4

Results and discussion

Suppressing of the skyrmion Hall effect using the VCMA effect

It is well known that due to the Magnus force the skyrmion produces a lateral drift (*i.e.*, SkHE),[8,56,57] causing the loss of the skyrmion signal. For the skyrmion-based diode, how to suppress the SkHE is undoubtedly an urgent problem to be solved. In the design, the VCMA effect induces the PMA at boundaries to be greater than that in the middle, confining the skyrmion to the middle of the nanotrack. Some experiments[64,65] show that the PMA energy generally changes linearly with the change in the applied electric field, and increases (positive voltage) or decreases (negative voltage) with the direction of the voltage. Note that the negative voltage is defined as an electron accumulation at the top surface of the multilayer here. In addition, since VCMA is an interface effect related to the thickness, the gradual change in PMA has been experimentally achieved by the thickness gradient of the film system.[54,66] Therefore, in the simulation, we designed six different schemes of PMA variation in the nanotrack, according to the voltage and the film thickness. The change in PMA is about ±10%, which could be achieved in experiments.

Fig. 2(a) shows the model adopted in the simulation, which is the CoPt nanotrack with a length of 400 nm. In this section, the effects of six different schemes of PMA variation, as shown in Fig. 2(b), on the skyrmion motion are studied. Schemes A and B apply a positive voltage to the upper and lower boundary of the nanotrack ($y \leq -20$ nm or $y \geq 20$ nm), so that the PMA K_b at the boundary is 1.1 times the original PMA K_c, $K_b = 1.1K_c$. In schemes C and D, the negative voltage is applied in the middle of the nanotrack (-20 nm $\leq y \leq 20$ nm), leading to the PMA K_m in the middle being 0.9 times the K_c, $K_m = 0.9K_c$. For schemes E and F, the voltage is added to the entire nanotrack, but the voltage directions at the boundary and in the middle are different, $K_b = 1.1K_c$ and $K_m = 0.9K_c$. In addition, schemes A, C and E are sharp transitions, while schemes B, D and F are smooth transitions.

Fig. 2(c and d) show the snapshots of the skyrmion motion at various simulation times under different schemes. On the nanotrack without the applied voltage, the skyrmion only stays for about 3.1 ns, as shown in Fig. 2(c). When $t = 3.1$ ns, the skyrmion that reaches the upper boundary due to the SkHE loses its topologically stable spin configuration and completely annihilates within 0.3 ns. At first, the motion of the skyrmion in scheme A is similar to that without the applied voltage, as shown in Fig. 2(d). However, when the skyrmion approaches

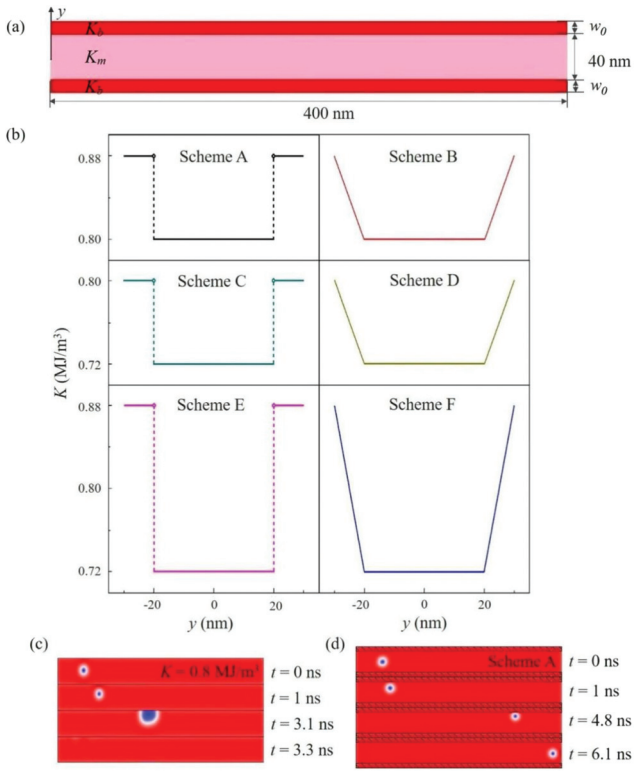

Fig. 2 (a) The model for simulating calculation. It is a 400 nm long and 0.4 nm thick CoPt nanotrack with $D = 3$ mJ m^{-2}. The PMA in red part is higher than that in pink part and the width w_0 is 0 nm∼40 nm. (b) Six different schemes for PMA variation on the nanotrack. Schemes A and B apply forward voltage at the upper and lower boundaries on the nanotrack ($y \leq -20$ nm or $y \geq 20$ nm), $K_b = 1.1K_c$. In schemes C and D, reverse voltage is applied in the middle of the nanotrack (-20 nm $\leq y \leq 20$ nm), $K_m = 0.9K_c$. For schemes E and F, voltage is applied throughout the nanotrack, but the voltage directions at the boundary and in the middle are different, $K_b = 1.1K_c$ and $K_m = 0.9K_c$. In addition, schemes A, C and E are sharp transitions, while schemes B, D and F are smooth transitions. For convenience, the midpoint of the nanotrack width is treated as the zero point for the y axis. (c and d) Simulation snapshots at various times t for the skyrmion driven by the spin current of 2 MA cm^{-2} on the nanotrack. (c) and (d) show the nanotrack without the applied voltage (*i.e.* $K_c = 0.8$ MJ m^{-3}) and in scheme A, respectively. The shaded section corresponds to the high-anisotropy region with a width of 10 nm. And the other five schemes of simulation results are similar to scheme A, which are not shown here.

the upper boundary, the high-anisotropy boundary has greater repulsion on the skyrmion than the geometric boundary, which limits the skyrmion to the nanotrack, then, the skyrmion oscillates in the x and y directions at the end of the nanotrack and finally returns to the center axis of the nanotrack width. It is worth noting that the oscillation behavior induced by the repulsion at the boundary has been observed in experiments.[56,59,67] In addition, the movement of the skyrmion in the other five schemes is basically the same as that shown in Fig. 2(d) (not shown in Fig. 2). This indicates that the high-anisotropy boundary formed by VCMA on the nanotrack can effectively suppress the SkHE. Note that the magnetic anisotropy gradient can also suppress the SkHE, where the

effect of the anisotropy gradient on the skyrmion motion has been reported.[68,69] The effect of the anisotropy gradient exerts a force on the skyrmion in the direction of the gradient. In schemes B, D and F, the force is along the $-y$ axis, which is opposite to the Magnus force that produces the SkHE, and it plays an important role in suppressing the SkHE.

Fig. 3(a and b) show relations between the maximum velocity v_x of the skyrmion along the x-axis and the width w_0 of the high-anisotropy boundary under six different schemes of PMA variation. And Fig. 3(c and d) show the ratio n between the depth d of the skyrmion entering the high-anisotropy boundary and the diameter d_s of the skyrmion as a function of the width w_0, $n = d_s/d$. If the depth d is less than 0, it means that the skyrmion does not enter the high-anisotropy boundary. The repulsion against the skyrmion is mainly caused by the high-anisotropy boundary and the geometric boundary. When the width w_0 increases at the beginning, the high-anisotropy boundary plays a dominant role and the repulsive

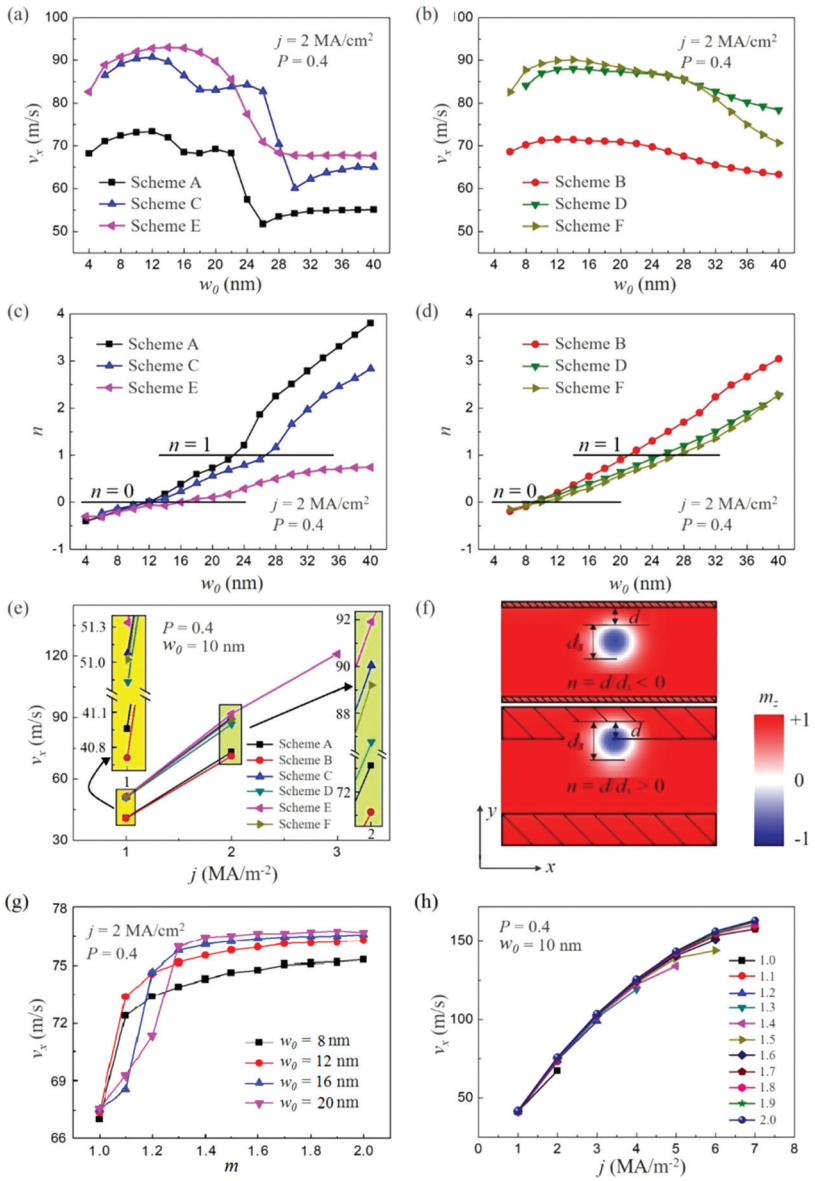

Fig. 3 (a and b) Calculated maximum velocities v_x of the skyrmion in the x-axis direction as a function of the width w_0 in six different schemes. (c and d) The ratio n of the depth d that the skyrmion enters the high-anisotropy boundary to the diameter d_s of the skyrmion as a function of the width w_0 on the nanotrack, $n = d/d_s$. If $n < 0$, it means that the skyrmion does not enter the high-anisotropy region. Otherwise, it means that some or all of the skyrmions enter, as shown in (f). The figure on the left is for schemes A, C and E, while the figure on the right is for schemes B, D and F. (e) The relation between the maximum velocities v_x along the x-axis direction and the driving current density j in six different schemes of PMA variation. Zoomed views of the curves around $j = 1$ MA cm^{-2} and $j = 2$ MA cm^{-2} are given. The relations of maximum velocity v_x *versus* (g) the ratio m at various high-anisotropy boundary widths w_0 and (h) the driving currents j at different ratios m. m is the ratio of PMA between the boundary and middle of the nanotrack in scheme A, $m = K_b/K_m = 1.0, 1.1, 1.2, \ldots 2.0$.

force increases. The suppression of the SkHE is enhanced and the lateral drift velocity of the skyrmion decreases, leading to the increase of v_x. At this stage, the skyrmion does not enter the high-anisotropy boundary in the process of movement [see the part in Fig. 3(c and d) where $n \leq 0$]. Then, as the width w_0 continues to increase, the geometric boundary dominates and the repulsion decreases. The skyrmion enters the high-anisotropy boundary little by little [see the part in Fig. 3(c and d) where $0 < n \leq 1$]. For schemes A, B, C, D, E and F, when w_0 is about 12 nm, 10 nm, 12 nm, 10 nm, 16 nm and 10 nm, respectively, the skyrmion starts to enter the high-anisotropy boundary. Due to the sharp transition of PMA (schemes A, C and E), the skyrmion that just enters and completely enters the high-anisotropy boundary diminishes significantly, and v_x reduces rapidly with the increase of w_0. Nevertheless, for the smooth transition of PMA (schemes B, D and F), the size and velocity v_x of the skyrmion entering the high-anisotropy boundary gradually decreases as w_0 increases. It can be illustrated that the sharp transition of PMA has a stronger suppression on the SkHE than the smooth transition of PMA. Finally, with the increase of w_0, the skyrmion totally enters the high-anisotropy boundary [see the part in Fig. 3(c and d) where $n > 1$]. And v_x gradually stabilizes under the sharp transition of PMA, but decreases quickly under the smooth transition of PMA.

The effect of the driving current density j on the maximum velocity v_x of the skyrmion is shown in Fig. 3(e). The motion of the skyrmion is faster in the sharp transition of PMA (schemes A, C and E) than that in the smooth transition (schemes B, D and F). On the nanotrack without the applied voltage (*i.e.*, K = 0.8 MJ m^{-3} in this work), the maximum velocity v_x is about 36.46 m s^{-1} for j = 1 MA cm^{-2}, and v_x is around 55.81 m s^{-1} when j = 2 MA cm^{-2}. It is worth noting that at the same current density j, the maximum velocity v_x under the six different schemes of PMA variation are bigger than it [see Table 2]. The movement of the skyrmion is not completely perpendicular to the x direction owing to the Magnus force. Consequently, the repulsion from the boundary is not entirely in the $-y$ direction, which has a component in the x direction instead and the velocity increases. This can also explain the changes in the velocity v_x shown in Fig. 3(a and b) where the skyrmion does not enter the high-anisotropy boundary. Moreover, the simulation results express that using VCMA can not only suppress the SkHE effectively, but also improve the velocity of the skyrmion.

Fig. 3(g) and (h) respectively show the relation of v_x with the ratio m and the driving current j in scheme (A). m is the ratio of PMA at the boundary to that in the middle on the nanotrack, $m = K_b/K_m$. As can be seen from Fig. 3(g), the enlargement of m does increase the velocity v_x when the driving current j is the same. The velocity v_x approaches a saturation value v_s (about 76.7 m s^{-1} in this work). It is very interesting that v_s depends on the parameters shown in Table 1, but not on the high-anisotropy boundary width w_0 (see Fig. S1 in the ESI†). The minimum m that gives the saturation value increases when the width w_0 decreases. It is about 1.6 for w_0 = 20 nm and 1.7 when w_0 = 16 nm. Furthermore, with the increase of the ratio m, it is more difficult for the skyrmion to enter the high-anisotropy boundary during the motion. It indicates that the high-anisotropy boundary plays a more important role than the geometric boundary when m is large. Beyond that, for $1.1 \leq m \leq 1.5$, the ratio m increases approximately in direct proportion to the maximum current that the skyrmion can successfully pass through the whole nanotrack. In Fig. 3(h), the maximum velocity v_x of the skyrmion can reach 163.1 m s^{-1}.

Realization of one-way motion function using the VCMA effect

For a skyrmion-based diode, in addition to avoiding the annihilation of the skyrmion, it is also necessary to achieve the one-way motion of the skyrmion. In the design, a high-anisotropy trapezoidal region is added in the middle of the nanotrack by VCMA, as shown schematically in Fig. 4(a). Fig. 4(b) shows the forward and reverse motion trajectories of the skyrmion on the nanotrack in scheme A. When t = 0 ns, the forward (or reverse) moving skyrmion is located at the left (or right) side of the nanotrack [see A_1 (or A_2) in Fig. 4(c)]. After that, owing to the SkHE, the skyrmion of the forward motion drifts in the $+y$ direction, reaching the trapezoidal barrier at t = 2.5 ns [see B_1 in Fig. 4(c)]. And the skyrmion of the reverse motion drifts in the $-y$ direction, touching the potential barrier at t = 2.2 ns [see B_2 in Fig. 4(c)]. Subsequently, the forward-moving skyrmion climbs up the left slope of the trapezoidal barrier [see C_1 in Fig. 4(c)]. The skyrmion gradually diminishes to pass above the barrier [see D_1 in Fig. 4(c)] and reaches the right side of the nanotrack [see F_1 in Fig. 4(c)]. However, the reverse-moving skyrmion also crawls along the trapezoidal right-angled edge [see C_2 in Fig. 4(c)], but it is bounced off [see D_2 in Fig. 4(c)]. Afterwards, the forward and reverse moving skyrmions have a precession at the right side of the nanotrack and near the barrier, respectively, as shown in Fig. 4(b). Finally, the reverse-moving skyrmion is stopped by the high-anisotropy trapezoidal region, while the forward-moving skyrmion bypasses it. This process, known as the one-

Table 2 The increased percentage for the maximum velocity v_x of the skyrmion in six different schemes of PMA variation, compared to the scheme without the applied voltage

The current density	Scheme A	Scheme B	Scheme C	Scheme D	Scheme E	Scheme F
1 MA cm^{-2}	12.34%	11.66%	40.10%	39.41%	40.81%	39.93%
2 MA cm^{-2}	31.08%	27.67%	61.94%	55.80%	64.90%	59.90%
3 MA cm^{-2}					109.20%	

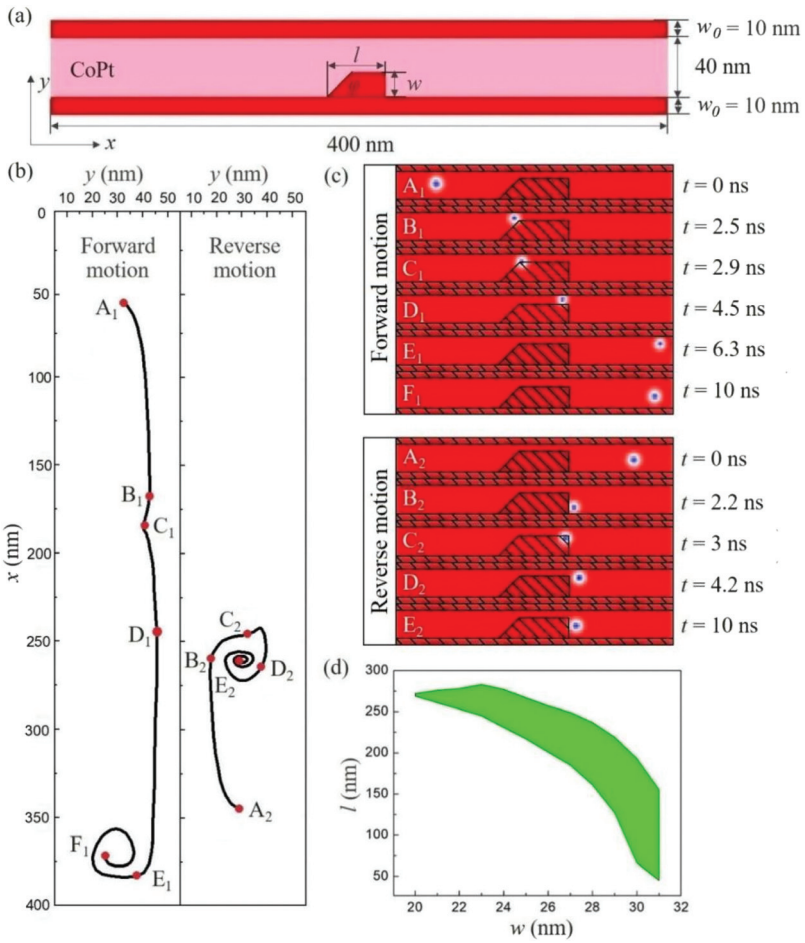

Fig. 4 (a) The model of simulating calculation. It is formed by adding a high-anisotropy trapezoidal region to the middle of the nanotrack based on Fig. 2(a). The red part represents the high-anisotropy region with the boundary width w_0 of 10 nm. (b) Trajectories of the skyrmion moving forward and reverse on the nanotrack in scheme A. (c) Snapshots of simulation at various positions marked by red dots in (b). The shaded section represents the high-anisotropy region, and the middle is a trapezoid with a length l of 100 nm, a width w of 30 nm, and a lower left corner φ of 45°. (d) Working window of the skyrmion-based diode with different widths w and lengths l of the high-anisotropy trapezoidal region. Green means that the diode is working properly. The simulation parameters are consistent with (b).

way motion of the skyrmion, can be realized by a high-anisotropy trapezoidal region on the nanotrack.

Fig. 4(d) shows the range of the length l and width w of the high-anisotropy trapezoidal region, in which the skyrmion can realize the one-way motion. When $w < 20$ nm, the skyrmion can reach the other side of the nanotrack whether in forward or reverse motion. The difference is that the skyrmion in the forward motion bypasses the trapezoidal region, while that in the reverse motion directly passes through it and gets annihilated. For 20 nm $\leq w \leq$ 31 nm, the realization of the one-way motion of the skyrmion depends on the length l. Moreover, as the width w increases, the working window of the skyrmion-based diode extends and the length l has a tendency to decrease. After the trapezoidal width w increases to 31 nm, the skyrmion of both motions is clogged. It can be seen that the working state of the skyrmion-based diode depends on the length l and width w of the trapezoidal region. And the range of the length l and width w that the skyrmion-based diode normally works is relatively wide.

The trapezoidal potential barrier gradually increases for the forward moving skyrmion. However, it increases suddenly when the skyrmion moves in the reverse direction. So the total energy of the skyrmion in the forward motion is significantly greater than that in the backward motion near the trapezoid. During the forward movement of the skyrmion, the total energy E_{total} has several sharp changes [see Fig. 5(a)]. These changes correspond to the critical moments shown in Fig. 4(c), when the skyrmion approaches both ends of the trapezoidal top and just arrives at the right side of the nanotrack. On the other hand, the demagnetization energy E_{demag} and DMI energy E_{DMI} increase [see Fig. 5(b)], while the exchange energy E_{exchange} and PMA energy E_{PMA} decrease [see Fig. 5(c)] in the process of the skyrmion passing over the trapezoid. It indicates that the total length of the magnetic domain wall reduces. Energies oscillate when $t > 6.3$ ns, which shows that the skyrmion changes regularly due to the repulsion and driving force. In addition, when the skyrmion passes the left end of the trapezoidal top, the increase in E_{PMA} dominates and

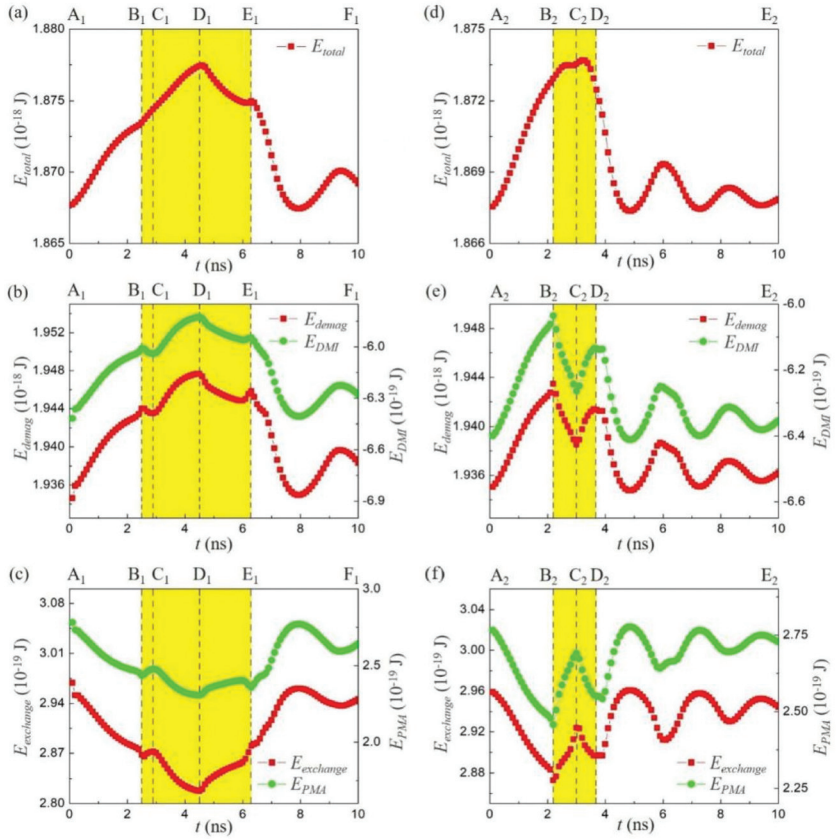

Fig. 5 (a) Total energy E_{total}, (b) demagnetization energy E_{demag} and DMI energy E_{DMI}, (c) exchange energy $E_{exchange}$ and anisotropic energy E_{PMA} as functions of the simulation time t for the skyrmion moving forward. (d) Total energy E_{total}, (e) demagnetization energy E_{demag} and DMI energy E_{DMI}, (f) exchange energy $E_{exchange}$ and anisotropic energy E_{PMA} as functions of the simulation time t for the skyrmion moving reverse. The calculation parameters are the same as that in Fig. 4(b). Vertical dashed lines indicate the selected times corresponding to snapshots shown in Fig. 4(c). Light yellow backgrounds indicate the time spans of the corresponding process.

E_{total} continues to increase as the skyrmion partially enters the high-anisotropy region [see C_1 Fig. 4(c)]. After the skyrmion in the reverse motion touches the trapezoid, E_{demag} and E_{DMI} reduce first and then increase [see Fig. 5(e)], while $E_{exchange}$ and E_{PMA} increase first and then decrease [see Fig. 5(f)]. However, E_{total} keeps increasing and decreasing at the moments B_2 and D_2 respectively [see Fig. 5(b)], because the influence of E_{PMA} on E_{total} is intensified when the skyrmion enters and leaves the trapezoidal high-anisotropy region. For t > 4.2 ns, energy variations of the skyrmion in the reverse motion are similar to those in the forward motion.

Apart from this, the PMA K_b at boundaries (including the trapezoid part) and the lower left corner φ of the trapezoid also affect the performance of the skyrmion-based diode. Fig. 6(a–c) are phase diagrams with various trapezoidal widths w and lengths l for one-way motion of the skyrmion under different φ values. The decrease of φ apparently expands the desirable range of the length l and width w. In other words, the smaller the angle φ, the easier it is for the forward-moving skyrmion to bypass the trapezoid. But it has little effect on the reverse-moving skyrmion. Fig. 6(d–f) show the effects of K_b on the phase diagrams of the length l and width w for the one-way motion of the skyrmion. It is found that the desirable range of the length l and width w expands as the PMA K_b increases when 0.8 MJ m^{-3} $\leq K_b \leq$ 0.88 MJ m^{-3}. Namely, the higher the K_b is, the harder it is for the reverse-moving skyrmion to bypass the trapezoid.

Indeed, the driving current j affects the one-way motion of the skyrmion. The critical current of the skyrmion-based diode is 2.05 MA cm^{-2} for the calculation parameter shown in Fig. 4. However, the driving current of the skyrmion-based diode in normal operation can be adjusted by PMA in the high-anisotropy region and other factors (see Fig. S2 of the ESI†). It is worth noting that the larger the PMA in the high-anisotropy region, the greater the driving current of the skyrmion-based diode in normal operation. When the driving current is high, the skyrmion passes through the trapezoid region, that is, the tunnel behavior. Continuing to increase the current, the skyrmion annihilates directly and does not enter the trapezoidal region.

In addition, the robustness of the results over the variation of the simulation parameters is discussed here. Three groups of trapezoidal length l and width w are randomly selected from the green part of Fig. 4(d). For w = 28 nm and l = 200 nm,

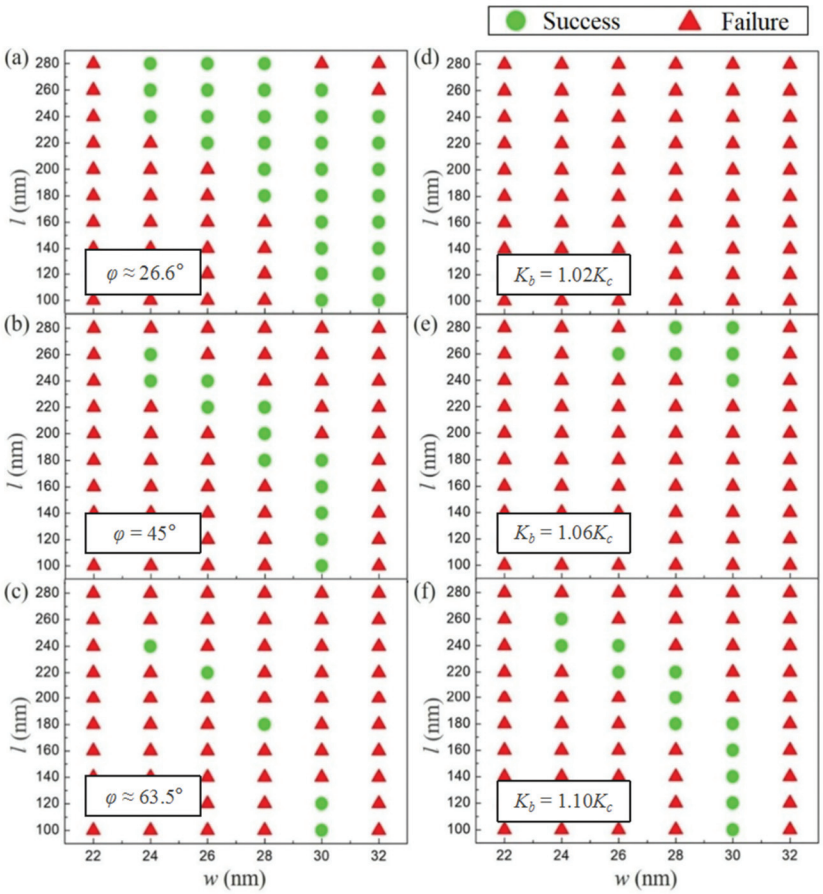

Fig. 6 (a–c) Phase diagrams for the one-way motion of the skyrmion with various trapezoid widths w and lengths l at the boundary PMA $K_b = 1.1K_c$. (a) $\varphi \approx 26.6°$ ($\tan\varphi = 1/2$), (b) $\varphi = 45°$ ($\tan\varphi = 1$)and (c) $\varphi \approx 63.5°$ ($\tan\varphi = 2$). (d–f) Calculated phase diagrams for the one-way motion of the skyrmion with different trapezoid widths w and lengths l at trapezoidal lower left corner $\varphi = 45°$. (d) $K_b = 1.02K_c$ ($K_b = 0.816$ MJ m^{-3}), (e) $K_b = 1.06K_c$ ($K_b = 0.848$ MJ m^{-3}) and (f) $K_b = 1.1K_c$ ($K_b = 0.880$ MJ m^{-3}). The skyrmion is driven by the spin current of 2 MA cm^{-2} on the nanotrack with $w_0 = 10$ nm in scheme A. The filled red triangle and the green circle stand for the failure and success of the one-way motion of the skyrmion, respectively.

when the saturation magnetization M_s, exchange stiffness A, anisotropy constant K, DMI constant D and damping coefficient α vary by about 17.2%, 26.7%, 12.5%, 6.7%, and 20% respectively, the one-way motion of the skyrmion can still be realized. But when the polarizability rate P increases more than 12.5%, the one-way motion of the skyrmion fails. The calculation results of the other two groups of trapezoidal length l and width w do not differ significantly, as shown in Fig. S3 in the ESI.† It can be seen from Fig. S3† that the one-way motion of the skyrmion has certain robustness over the variation of the simulation parameters, which proves that the design has certain feasibility in experiments.

Actually, the voltage can form or eliminate the skyrmion, which has been illustrated by experiments.[70–72] In other words, the positive (negative) voltage can promote (inhibit) the formation of the skyrmion. Therefore, this work does not discuss too much about the influence of voltage on the generation of the skyrmion, but focuses on the influence of voltage on its motion. At present, some experimental studies have shown that in addition to the magnetic anisotropy, the DM interaction is also affected by the voltage in heavy metal/ferromagnet/insulator heterostructures.[72,73] T. Srivastava *et al.* reported that a large variation of interfacial DMI and PMA can be induced by voltage gating using Brillouin Light Spectroscopy (BLS), which decrease (increase) with the negative (positive) voltage.[72] Hence, we discuss the motion of the skyrmion when the voltage affects both PMA and DMI, as shown in Fig. S4 in the ESI.† The results show that the large-DMI boundary is not conducive to the inhibition of the SkHE on the nanotrack. And the structure of the skyrmion is destroyed and rapidly annihilates once the skyrmion enters the large-DMI boundary. But when m is large, it also increases the velocity v_x of the skyrmion along the nanotrack, which is weaker than the high-anisotropy boundary.

Conclusions

In summary, a feasible skyrmion-based diode model using VCMA is devised and the dynamic behavior of the skyrmion is studied in the model. Here, we discuss the motion of the skyrmion under six different schemes of PMA variation according

to the voltage and the film thickness. The research results show that the high-anisotropy boundaries of the nanotrack can effectively suppress the SkHE, preventing the loss of skyrmion information. What's more, they can also improve the velocity of the skyrmion, which is improved by at least 11.66% in the simulation. On the other hand, the one-way motion of the skyrmion can be realized by a high-anisotropy trapezoidal region on the nanotrack. The forward-moving skyrmion can bypass the region, while the reverse-moving skyrmion is clogged nearby. In this section, we not only analyze the energy variation during the movement of the skyrmion, but also find that the geometric parameters of the high-anisotropy trapezoid and so on have effects on the diode. Furthermore, the prototype proposed in our work can realize the functional transformation of the racetrack memory and diode through the high-anisotropy trapezoidal region.

Conflicts of interest

The authors declare no conflicts of interest.

Acknowledgements

G. Z. acknowledges the support from the National Natural Science Foundation of China (Grant No. 51771127, 51571126 and 51772004) and the Scientific Research Fund of Sichuan Provincial Education Department (Grant No. 18TD0010 and 16CZ0006). Y. Z. acknowledges the support from the President's Fund of CUHKSZ, the Longgang Key Laboratory of Applied Spintronics, the National Natural Science Foundation of China (Grant No. 11974298 and 61961136006), the Shenzhen Fundamental Research Fund (Grant No. JCYJ20170410171958839), and the Shenzhen Peacock Group Plan (Grant No. KQTD20180413181702403).

References

1 S. Mühlbauer, B. Binz, F. Jonietz, C. Pfleiderer, A. Rosch, A. Neubauer, R. Georgii and P. Böni, *Science*, 2009, **323**, 915–919.
2 X. Z. Yu, Y. Onose, N. Kanazawa, J. H. Park, J. H. Han, Y. Matsui, N. Nagaosa and Y. Tokura, *Nature*, 2010, **465**, 901–904.
3 S. Heinze, K. von Bergmann, M. Menzel, J. Brede, A. Kubetzka, R. Wiesendanger, G. Bihlmayer and S. Blugel, *Nat. Phys.*, 2011, **7**, 713–718.
4 M. Heide, G. Bihlmayer and S. Blügel, *Phys. Rev. B: Condens. Matter Mater. Phys.*, 2008, **78**, 140403.
5 T. H. R. Skyrme, *Proc. R. Soc. A*, 1961, **260**, 127–138.
6 C. Peiderer and A. Rosch, *Nature*, 2010, **465**, 880–881.
7 X. Z. Yu, N. Kanazawa, Y. Onose, K. Kimoto, W. Z. Zhang, S. Ishiwata, Y. Matsui and Y. Tokura, *Nat. Mater.*, 2011, **10**, 106–109.
8 N. Nagaosa and Y. Tokura, *Nat. Nanotechnol.*, 2013, **8**, 899–911.
9 M. Beg, R. Carey, W. Wang, D. Cortés-Ortuño, M. Vousden, M. A. Bisotti, M. Albert, D. Chernyshenko, O. Hovorka, R. L. Stamps and H. Fangohr, *Sci. Rep.*, 2013, **5**, 17137.
10 J. Sampaio, V. Cros, S. Rohart, A. Thiaville and A. Fert, *Nat. Nanotechnol.*, 2013, **8**, 839–844.
11 A. Fert, V. Cros and J. Sampaio, *Nat. Nanotechnol.*, 2013, **8**, 152–156.
12 S. S. P. Parkin, M. Hayashi and L. Thomas, *Science*, 2008, **320**, 190–194.
13 A. Thiaville, S. Rohart, E. Jue, V. Cros and A. Fert, *Europhys. Lett.*, 2012, **100**, 57002.
14 A. Brataas, A. D. Kent and H. Ohno, *Nat. Mater.*, 2012, **11**, 372–381.
15 Y. Zhou and M. Ezawa, *Nat. Commun.*, 2014, **5**, 4652.
16 X. Xing, P. W. T. Pong and Y. Zhou, *J. Appl. Phys.*, 2016, **120**, 203903.
17 H. Dery, P. Dalal, L. Cywinski and L. J. Sham, *Nature*, 2007, **447**, 573–576.
18 J. Zázvorka, F. Jakobs, D. Heinze, N. Keil, S. Kromin, S. Jaiswal, K. Litzius, G. Jakob, P. Virnau, D. Pinna, K. Everschor-Sitte, L. Rózsa, A. Donges, U. Nowak and M. Kläui, *Nat. Nanotechnol.*, 2019, **14**, 658–661.
19 T. Nozaki, Y. Jibiki, M. Goto, E. Tamura, T. Nozaki, H. Kubota, A. Fukushima, S. Yuasa and Y. Suzuki, *Appl. Phys. Lett.*, 2019, **114**, 012402.
20 A. Fert, N. Reyren and V. Cros, *Nat. Rev. Mater.*, 2017, **2**, 17031.
21 W. Kang, Y. Huang, X. Zhang, Y. Zhou and W. Zhao, *Proc. IEEE*, 2016, **104**, 2040–2061.
22 W. Koshibae, Y. Kaneko, J. Iwasaki, M. Kawasaki, Y. Tokura and N. Nagaosa, *Jpn. J. Appl. Phys.*, 2015, **54**, 053001.
23 X. Liang, L. Zhao, L. Qiu, S. Li, L. H. Ding, Y. H. Feng, X. Zhang, Y. Zhou and G. P. Zhao, *Acta Phys. Sin.*, 2018, **67**, 137510.
24 S. Parkin and S. H. Yang, *Nat. Nanotechnol.*, 2015, **10**, 195–198.
25 S. S. P. Parkin, Unidirectional racetrack memory device, *US patent* 7551469, 2009.
26 X. Zhang, Y. Zhou, M. Ezawa, G. P. Zhao and W. Zhao, *Sci. Rep.*, 2015, **5**, 11369.
27 X. C. Zhao, R. Ren, R. Xie and Y. Liu, *Appl. Phys. Lett.*, 2018, **112**, 252402.
28 J. Xia, Y. Huang, X. Zhang, W. Kang, C. Zheng, X. Liu, W. Zhao and Y. Zhou, *J. Appl. Phys.*, 2017, **122**, 153901.
29 H. T. Fook, W. L. Gan and W. S. Lew, *Sci. Rep.*, 2016, **6**, 21099.
30 X. Zhang, M. Ezawa and Y. Zhou, *Sci. Rep.*, 2014, **5**, 9400.
31 H. Dery, P. Dalal, L. Cywinski and L. J. Sham, *Nature*, 2007, **447**, 573–576.
32 L. C. Shen, J. Xia, G. P. Zhao, X. Zhang, M. Ezawa, O. A. Tretiakov, X. X. Liu and Y. Zhou, *Appl. Phys. Lett.*, 2019, **114**, 042402.
33 F. Garcia-Sanchez, J. Sampaio, N. Reyren, V. Cros and J. V. Kim, *New J. Phys.*, 2016, **18**, 075011.
34 S. F. Zhang, J. B. Wang, Q. Zheng, Q. Zhu, X. Liu, S. Chen, C. Jin, Q. Liu, C. Jia and D. Xue, *New J. Phys.*, 2015, **17**(2), 023061.

35 Y. Huang, W. Kang, X. Zhang, Y. Zhou and W. Zhao, *Nanotechnology*, 2017, **28**, 08LT02.

36 G. Finocchio, M. Ricci, R. Tomasello, A. Giordano, M. Lanuzza, V. Puliafito, P. Burrascano, B. Azzerboni and M. Carpentieri, *Appl. Phys. Lett.*, 2015, **107**, 262401.

37 X. Zhang, G. P. Zhao, H. Fangohr, J. P. Liu, W. X. Xia and J. Xia, *Sci. Rep.*, 2014, **5**, 7643.

38 X. Z. Yu, N. Kanazawa, W. Z. Zhang, T. Nagai, T. Hara, K. Kimoto, Y. Matsui, Y. Onose and Y. Tokura, *Nat. Commun.*, 2012, **3**, 988.

39 A. Hrabec, J. Sampaio, M. Belmeguenai, I. Gross, R. Weil, S. M. Chérif, A. Stashkevich, V. Jacques, A. Thiaville and S. Rohart, *Nat. Commun.*, 2017, **8**, 15765.

40 J. C. Sankey, Y. T. Cui, J. Z. Sun, J. C. Slonczewski, R. A. Buhrman and D. C. Ralph, *Nat. Phys.*, 2008, **4**, 67–71.

41 W. Skowroński, T. Nozaki, Y. Shiota, S. Tamaru, K. Yakushiji, H. Kubota, A. Fukushima, S. Yuasa and Y. Suzuki, *Appl. Phys. Express*, 2015, **8**, 053003.

42 X. Li, K. Fitzell, D. Wu, C. T. Karaba, A. Buditama, G. Yu, K. L. Wong, N. Altieri, C. Grezes, N. Kioussis, S. Tolbert, Z. Zhang, J. P. Chang, P. K. Amiri and K. L. Wang, *Appl. Phys. Lett.*, 2017, **110**, 052401.

43 T. Hirai, T. Koyama, A. Obinata, Y. Hibino, K. Miwa, S. Ono, M. Kohda and D. Chiba, *Appl. Phys. Express*, 2016, **9**, 063007.

44 D. Chiba, M. Kawaguchi, S. Fukami, N. Ishiwata, K. Shimamura, K. Kobayashi and T. Ono, *Nat. Commun.*, 2012, **3**, 888.

45 Y. Hibino, T. Koyama, A. Obinata, T. Hirai, S. Ota, K. Miwa, S. Ono, F. Matsukura, H. Ohno and D. Chiba, *Appl. Phys. Lett.*, 2016, **109**, 082403.

46 Y. Hayashi, Y. Hibino, F. Matsukura, K. Miwa, S. i. Ono, T. Hirai, T. Koyama, H. Ohno and D. Chiba, *Appl. Phys. Express*, 2018, **11**, 013003.

47 T. Kawabe, K. Yoshikawa, M. Tsujikawa, T. Tsukahara, K. Nawaoka, Y. Kotani, K. Toyoki, M. Goto, M. Suzuki, T. Nakamura, M. Shirai, Y. Suzuki and S. Miwa, *Phys. Rev. B: Condens. Matter Mater. Phys.*, 2017, **96**, 220412(R).

48 C. G. Duan, J. P. Velev, R. F. Sabirianov, Z. Zhu, J. Chu, S. S. Jaswal and E. Y. Tsymbal, *Phys. Rev. Lett.*, 2008, **101**, 137201.

49 K. Nakamura, R. Shimabukuro, Y. Fujiwara, T. Akiyama, T. Ito and A. J. Freeman, *Phys. Rev. Lett.*, 2009, **102**, 187201.

50 M. Tsujikawa and T. Oda, *Phys. Rev. Lett.*, 2009, **102**, 247203.

51 F. Ando, M. Ishibashi, T. Koyama, Y. Shiota, T. Moriyama, D. Chiba and T. Ono, *Appl. Phys. Lett.*, 2018, **113**, 252402.

52 S. Peng, S. Li, W. Kang, J. Zhou, N. Lei, Y. Zhang, H. Yang, X. Li, P. K. Amiri, K. L. Wang and W. Zhao, *Appl. Phys. Lett.*, 2017, **111**, 152403.

53 K. Nakamura, T. Akiyama, T. Ito, M. Weinert and A. J. Freeman, *Phys. Rev. B: Condens. Matter Mater. Phys.*, 2010, **81**, 220409(R).

54 T. Maruyama, Y. Shiota, T. Nozaki, K. Ohta, N. Toda, M. Mizuguchi, A. A. Tulapurkar, T. Shinjo, M. Shiraishi, S. Mizukami, Y. Ando and Y. Suzuki, *Nat. Nanotechnol.*, 2009, **4**, 158–161.

55 A. J. Tan, M. Huang, C. O. Avci, F. Büttner, M. Mann, W. Hu, C. Mazzoli, S. Wilkins, H. L. Tuller and G. S. D. Beach, *Nat. Mater.*, 2018, **18**, 35–41.

56 W. Jiang, X. Zhang, G. Yu, W. Zhang, X. Wang, M. B. Jungfleisch, J. E. Pearson, X. Cheng, O. Heinonen, K. L. Wang, Y. Zhou, A. Hoffmann and S. G. E. te Velthuis, *Nat. Phys.*, 2017, **13**, 162–169.

57 K. Litzius, I. Lemesh, B. Krüger, P. Bassirian, L. Caretta, K. Richter, F. Büttner, K. Sato, O. A. Tretiakov, J. Förster, R. M. Reeve, M. Weigand, L. Bykova, H. Stoll, G. Schütz, G. S. D. Beach and M. Kläui, *Nat. Phys.*, 2017, **13**, 170–175.

58 X. Zhang, Y. Zhou and M. Ezawa, *Nat. Commun.*, 2006, **7**, 10293.

59 P. Lai, G. P. Zhao, H. Tang, N. Ran, S. Q. Wu, J. Xia, X. Zhang and Y. Zhou, *Sci. Rep.*, 2017, **7**, 45330.

60 I. Purnama, W. L. Gan, D. W. Wong and W. S. Lew, *Sci. Rep.*, 2015, **5**, 10620.

61 G. W. Neudeck, *The PN Junction Diode*, Addison-Wesley, Reading, MA, 1989.

62 K. S. Lee, D. H. Jeong, H. S. Han and N. K. Kim, Skyrmion diode and method of manufacturing the same, US 20170256633A1, 2017.

63 R. Tomasello, E. Martinez, R. Zivieri, L. Torres, M. Carpentieri and G. Finocchio, *Sci. Rep.*, 2014, **4**, 6784.

64 A. J. Schellekens, A. van den Brink, J. H. Franken, H. J. M. Swagten and B. Koopmans, *Nat. Commun.*, 2012, **3**, 847.

65 Y. Shiota, S. Murakami, F. Bonell, T. Nozaki and Y. Suzuki, *Appl. Phys. Express*, 2011, **4**, 043005.

66 C. Ma, X. Zhang, J. Xia, M. Ezawa, W. Jiang, T. Ono, S. N. Piramanayagam, A. Morisako, Y. Zhou and X. Liu, *Nano Lett.*, 2019, **19**, 353–361.

67 H. Du, R. Che, L. Kong, X. Zhao, C. Jin, C. Wang, J. Yang, W. Ning, R. Li, C. Jin, X. Chen, J. Zang, Y. Zhang and M. Tian, *Nat. Commun.*, 2015, **6**, 8504.

68 R. Tomasello, S. Komineas, G. Siracusano, M. Carpentieri and G. Finocchio, *Phys. Rev. B: Condens. Matter Mater. Phys.*, 2018, **98**, 024421.

69 L. C. Shen, J. Xia, G. P. Zhao, X. Zhang, M. Ezawa, O. A. Tretiakov, X. Liu and Y. Zhou, *Phys. Rev. B: Condens. Matter Mater. Phys.*, 2018, **98**, 134448.

70 M. Schott, A. Bernand-Mantel, L. Ranno, S. Pizzini, J. Vogel, H. Béa, C. Baraduc, S. Auffret, G. Gaudin and D. Givord, *Nano Lett.*, 2017, **17**, 3006–3012.

71 P.-J. Hsu, A. Kubetzka, A. Finco, N. Romming, K. von Bergmann and R. Wiesendanger, *Nat. Nanotechnol.*, 2017, **12**, 123–126.

72 T. Srivastava, M. Schott, R. Juge, V. Křižáková, M. Belmeguenai, Y. Roussigné, A. B. Mantel, L. Ranno, S. Pizzini, S.-M. Chérif, A. Stashkevich, S. Auffret, O. Boulle, G. Gaudin, M. Chshiev, C. Baraduc and H. Béa, *Nano Lett.*, 2018, **18**, 4871–4877.

73 J. Suwardy, K. Nawaoka, J. Cho, M. Goto, Y. Suzuki and S. Miwa, *Phys. Rev. B: Condens. Matter Mater. Phys.*, 2018, **98**, 144432.